In situ investigation of MgO nanocube deformation at room temperature

Inas Issa, Jonathan Amodeo, Julien Réthoré, Lucile Joly-Pottuz, Claude Esnouf, Julien Morthomas, Michel Perez, Jérome Chevalier, Karine Masenelli-Varlot

In situ investigation of MgO nanocube deformation at room temperature

I. Issa[1,2], J. Amodeo[1]*, J. Réthoré[2], L. Joly-Pottuz[1], C. Esnouf[1], J. Morthomas[1], M. Perez[1], J. Chevalier[1] and K. Masenelli-Varlot[1]

[1] *MATEIS, CNRS UMR5510, Université de Lyon, INSA-Lyon, F-69621 Villeurbanne Cedex, France*

[2] *LAMCOS, CNRS UMR5259, Université de Lyon, INSA-Lyon, F-69621 Villeurbanne Cedex, France*

(*) Corresponding author:

Dr. Jonathan Amodeo
Laboratoire MATEIS - UMR CNRS 5510
Groupe METAL, groupe CERA
25 avenue Jean Capelle
Bat. St. Exupéry, 2ème étage
69621 Villeurbanne Cedex, France
Tel: 04 72 43 82 35
Fax: 04 72 43 85 39
e-Mail: jonathan.amodeo@insa-lyon.fr

In situ investigation of MgO nanocube deformation at room temperature

Abstract

The mechanical behaviour of <100>-oriented MgO nanocubes is investigated using *in situ* TEM compression tests at room temperature and molecular dynamics simulations. Experiments show high strength and ductility in addition to specific deformation mechanisms interpreted by the simulation. The nucleation and the propagation of ½<110>{110} dislocations are at the onset of the plastic deformation. The different deformation processes as well as the possible formation of a dislocation network during compression are discussed.

Keywords: MgO, *in situ* TEM, nanoparticles, molecular dynamics, nanomechanics, dislocations

I Introduction

Nanocrystalline (NC) ceramics are of particular interest because of their high mechanical characteristics *e.g.*, high hardness, crack propagation resistance, superplastic deformation at moderate temperatures, better than their conventional polycrystalline counterparts [1,2]. Therefore, NC ceramics are increasingly used for their mechanical properties, as example in the field of modern orthopaedic surgery where they are employed as femoral heads or acetabular cups, in replacement of metallic alloys, to extend medical prosthesis lifetime. Their use indeed reduces wear rates and ion release, presumed to be responsible for inflammatory reactions [3,4]. In this context, one way to enhance the mechanical properties of post-processed NC ceramics and thereby optimize their compaction and sintering processes is to improve the global understanding of the mechanics of ceramic nanoparticles. As for NC ceramics, the mechanical properties of nano-objects as pillars, particles or wires have recently drawn intensive scientific attention mainly through their high achievable yield

strength and ductility [5]. Owing to the characteristic sizes of such objects, *in situ* mechanical tests in a transmission electron microscope (TEM) or in a scanning electron microscope (SEM) have revealed to give valuable pieces of information regarding the deformation mechanisms [6,7]. Deep in the submicrometer scale, size phenomena influence elastic properties of nanowires (NWs) and nanoparticles through the combination of surface and core effects in both the experiments and atomistic simulations [8,9]. This size effect involves also the plastic deformation regime for whom few theories based on the single-arm dislocation source model or the dislocation nucleation/starvation model [10,11] still try to provide a unique description of the now well-known principle “smaller is stronger”. Nevertheless, most of these studies are carried on metals, especially face-centered cubic (FCC), and only few works have been dedicated to ceramics [12-15]. Calvie ~~*et al.*~~ and collaborators have recently reported *in situ* compression tests in the TEM of a γ-alumina Al_2O_3 nanospheres [14]. The main feature of this study is that the sample undergoes wide and homogeneous plastic deformation, as observed in metallic [16,17], intermetallic [18] or silicon [19,20] nanoparticles. A detailed mechanical analysis based on digital image correlation (DIC) and finite elements simulations allowed the determination of a mechanical constitutive law [21]. However, the identification of elementary mechanisms responsible for plastic deformation in γ-Al_2O_3 nanospheres could not be determined *in situ*. In particular, no dislocation could be observed experimentally. This lack was primarily attributed to the spherical geometry of the sample and to the diffraction conditions. Furthermore, γ-Al_2O_3 is not a stable phase at the macroscopic scale what restricts drastically the comparison of its mechanical properties to the other bulk-type alumina (α-phase). At this point, it has to be mentioned that dislocations could successfully be observed *in situ* in silver nanoparticles [22] but compression axis could not be clearly determined from the images and the interpretation remained qualitative.

Here we propose to reach further the investigation of the mechanical behaviour of single crystalline ceramic nanoparticles using *in situ* TEM compression tests and molecular dynamics (MD) simulations applied to magnesium oxide (MgO).

MgO is an ionic ~~model~~ ceramic with the B1 crystalline structure which has been widely studied in the past decades for its potential application as a refractory material (T_f > 3000 K). MgO is also considered as a model material for dislocation properties analysis in B1-structured alkali halides and other ionic ceramics (*e.g.*, NaCl, LiF, KCl, CaO, etc.) [23]. As most ceramic materials do under compression, bulk MgO single crystals accommodate only a slight amount of strain before failure (~7% for <100>-oriented samples) at room temperature (RT), while larger deformation is reached at higher temperature [24,25]. In bulk MgO, plastic strain is governed either by lattice friction, solution hardening or dislocation-dislocation interactions depending on the investigated temperature range [26-28]. At RT, lattice friction competes with solution hardening on the two main slip system families ½<110>{110} and ½<110>{100} of the crystalline structure. {111} and {112} slips have been observed only in rare and exotic cases [29-31]. ½<110>{110} dislocation glide involves the nucleation of kink-pairs, typical of the lattice friction regime. This specific process leads to a characteristic dislocation microstructure made of rate-controlling long screw dislocations [32,33] which are also observed in body-centered cubic (BCC) metals at low temperature [34,35]. Above a transition temperature (*ca.* 600 K for ½<110>{110} slip systems and 1500 K for ½<110>{100}), lattice friction is overcome and plastic strain is accommodated by curved dislocations [36,37], ruled by the strength of dislocation-dislocation "forest" interactions [38,39]. In addition to well-known mechanical properties, MgO is stable at small scale and high pressure [40,41]. Finally, MgO nanoparticles can be easily synthetized from different methods leading to perfectly well-shaped nanocubes [42,43]. This sharp geometry permits to easily define a standard [001] compression axis, simplify the identification of slip systems and reduce the misorientation troubles commonly observed in nanosphere compression tests.

In this study, we report *in situ* compression experiments in the TEM and MD compression simulations of MgO nanocubes at RT. Simulations are performed to investigate elementary deformation mechanisms at the atomic scale and corroborate experimental observations.

II Materials and methods

II.1 Nanocube experimental synthesis and characterization

Magnesium oxide nanocubes were prepared by burning commercial Magnesium chips (4-30 mesh) in air as described in the pioneer work of Heidenreich [44]. This specific method is known to produce perfectly cubic-shaped nanoparticles down to sizes of a few nm. The smoke particles were caught directly on three substrates: a glass substrate for SEM imaging, a TEM grid (Cu 300-mesh covered by a holey carbon film) and the nanocompression sapphire substrate.

Primary characterisations were carried out by SEM, high resolution TEM (HRTEM) and weak beam dark field (WBDF) TEM. SEM images were acquired on a Zeiss Supra 55VP microscope. The acceleration voltage was fixed to 1 kV and images were acquired with a secondary electron Everhardt-Thornley detector. For the HRTEM observations, a JEOL 2010F TEM microscope equipped with a field emission gun and operating at 200 kV was used. Images were recorded using a Gatan Orius 200 CCD camera. Energy-dispersive spectroscopy (EDS) was performed using an 80 mm^2 SSD detector from Oxford Instruments. Finally, WBDF characterisations were carried out on a JEOL 200CX microscope, equipped with a tungsten filament that operates at 200 kV. Images were acquired with the wave [220], that allows the detection of dislocations in the (101), $(10\bar{1})$, (011) and $(01\bar{1})$ slip planes. Under such conditions, dislocations can be imaged as narrow lines which are approximately 10-15 nm wide [45].

A typical SEM image of the collected smoke is displayed figure 1a. Particles consist mostly of sharp nanocubes with edge sizes ranging between 20 nm and 300 nm. EDS spectra (not displayed) acquired during HRTEM observations indicate that the nanocubes are exclusively

composed of MgO (99.9 ± 0.1 at.%). Particles are single crystals, as shown in the HRTEM image of figure 1b. The surfaces of the nanocubes are crystalline as well and are oriented along the <100> directions, as shown by the electronic diffraction patterns, figure 1b. Regarding the importance that dislocations have during all stages of plastic deformation, a large number of MgO nanocubes were characterized by WBDF before any mechanical test. Figure 1c displays a WBDF image of two MgO nanocubes. The image shows no bulk lattice defect such as dislocations, grain boundaries or twinning. Contrasts were only observed at the contact points of the nanocubes, and were attributed to the stress field induced by the elastic compression of the lattice [46]. None of the imaged nanocubes were found to contain bulk lattice defects. In the following, similar samples used for *in situ* nanocompression testing will thus be considered as initially dislocation-free.

II.2 In situ TEM nanocompression

Pristine MgO nanocubes were deposited onto a 75 μm-thick sapphire substrate by passing the substrate in the smoke during synthesis. This method precludes the use of solvents that may modify the surface structure of MgO samples [47]. Since the nanocubes exhibit <100> surfaces, the compression axis is expected to be parallel to [001].

In situ nanocompression tests were carried out using a dedicated sample holder from Nanofactory Instruments, fitted in a JEOL 2010F microscope operating at 200 kV accelerating voltage. The sample holder was equipped with a truncated diamond tip (flattened area of about 0.25 μm^2) and a load cell (maximum load of 3 mN), as shown figure 1d. Particles were positioned on the substrate, displaced toward the tip during compression at a controlled displacement rate of 2 nm/s that is equivalent to an engineering strain rate of 0.02 s^{-1} for a 100 nm nanocube.

The longitudinal displacement of the substrate was determined using DIC. For this purpose, a rigorous comparison of grey level transitions between the tip, the samples and the substrate has been performed on successive images. DIC allows arbitrary displacement

fields to be estimated with a sub-pixel resolution (about 1/100 pixel). The distance measured between substrate and diamond tip edges corresponds to the instant size of the sample. Furthermore, not only the longitudinal displacement but also the lateral deformation was obtained. As the longitudinal and lateral deformations were synchronized on-the-fly with the force value, true stress and true strain were deduced considering that lateral deformations were equivalent in both directions. The true strain is defined as $\ln(L/L_0)$, where L is the instantaneous position and L_0 is the initial position of the substrate with respect to the tip *i.e.*, the initial nanocube size. The true stress is defined as the ratio between the instant force measured by the sensor and the effective cube surface inferred from the DIC calculation.

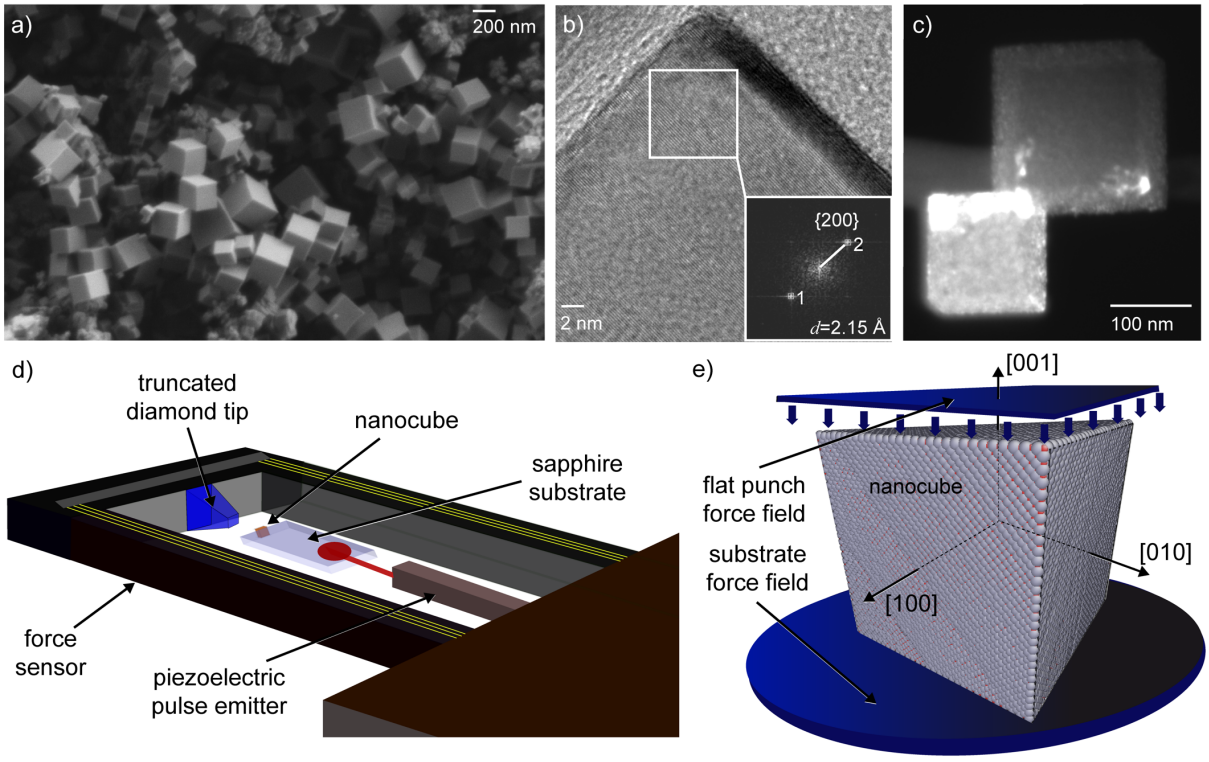

Fig. 1 *(Color online) (a) SEM image of smoked MgO nanocubes. (b) HRTEM image of a nanocube. In the inset, the diffraction pattern shows {200} crystallographic planes with a lattice spacing of about 2.15 Å. The sample is fully crystalline and surfaces are oriented along the <100> directions. (c) WBDF TEM image of two nanocubes free of bulk lattice defects. Only few contrasts due to contacts between adjacent cubes can be observed. (d) Scheme of the nanocompression experimental set-up. For the sake of clarity, the size of the sample has been widely increased compared to other components. (e) Scheme of the MD*

nanocompression simulation set-up, made of two force fields to respectively sustain and compress the nanocube.

II.3 Computational methods

MD simulations were performed to investigate elementary deformation mechanisms of initially dislocation-free MgO nanocubes under compression at RT using the LAMMPS code [48]. Atomic interactions were described using a rigid ion model that included a Buckingham term in addition to long-range Coulombic interactions. Here we used the Ball and Grimes partial charges parameterization [49] successfully employed to describe surface diffusion [49], elastic constants and dislocation properties [50], which are considered as key points for interatomic potential transferability towards nanomechanical test simulations. We used a cut-off parameter of 8 Å for short-range interactions. Full long-range interactions between charges in compression simulations were computed using the multi-level summation method (MSM) solver [51]. MSM relative error in per-atom forces from 10^{-4} to 10^{-8} were tested without significant outcome on the simulation results. Cubic samples with edge lengths from 4.2 nm to 12.7 nm were shaped with free surfaces oriented along the <100> directions as suggested by the experiment. The MD compression tests of MgO nanocubes were performed using the following procedure. First, the structure of the nanocubes was optimized using conjugate gradient and the FIRE algorithm [52]. Next, the samples were equilibrated during 30 ps in the NVE ensemble down to 300 K. Then, we used the Nosé-Hoover thermostat [53] for 50 ps equilibration in the NVT canonical ensemble. Finally, the compression tests were performed using two external potentials (see figure 1e) which model an infinite flat punch and the substrate [54,55]. To model uniaxial compression along the [001] direction, the top indenter was subjected to a constant displacement rate equivalent to an engineering strain rate of 10^{8} s^{-1}. The bottom potential was kept fixed to sustain the sample. During compression simulations, time steps down to 2 fs were used and the Nosé-Hoover thermostat imposed a

temperature of 300 K. Note that sample size, strain rate and other simulation parameters were chosen regarding settings generally adopted in the case of the embedded-atom method (EAM) for metals [17], what involves a significant increase of the cpu costs due to long-range Coulombic interactions in this study. The true strain was calculated as in the experiment (see previous section) and the compressive stress was computed as the ratio between the force experienced by the indenter and the instantaneous maximum contact area drawn by the last upper atomic layers. Simulations were analysed using *AtomViewer* [56], a tool which combines a modified bond-angle method [57] to identify crystalline structures, a Nye-tensor analysis for dislocation Burgers vector definition [58] and a skeletonization algorithm for dislocation reconstruction [59].

An Ewald summation method [60] with a radius of 12 Å was used for the calculation of bulk material properties that involved periodic boundary conditions *e.g.*, lattice parameter, elastic constants and generalized stacking fault (GSF) energies [61]. We used the same short-range interaction cut-off (8 Å) for bulk material properties and nanocompression simulations. GSF energies were computed using the full periodic method described in Gouriet *et al.* (2014) study [62] to avoid artefacts induced by charged surfaces. Calculations were performed along the ½<110> Burgers vector direction for {110}, {100} and {111} planes. Simulation cells were chosen large enough, especially along the orientation of the stacking fault normal, to reduce the interactions between fault periodic replicas and minimize long-range Coulombic effects. The initial size of the simulation cells are 1.79 nm*1.69 nm*14.29 nm, 1.79 nm*1.79 nm*14.31 nm and 1.49 nm*1.55 nm*27.71 nm respectively for {110}, {100} and {111} GSF calculations.

III Results

III.1 Mechanical behaviour of MgO nanocubes

The mechanical response of a 140 nm edge size MgO nanocube is displayed on figure 2a. The compression test is composed of five successive load-unload cycles. In addition to the

stress-strain curve, four ~~on the fly~~ *on-the-fly* images are presented figure 2b-e for true strain of about ε=1.2%, ε =18.7%, ε =49.7% and ε =78.9% respectively. The sample is deformed up to ε =79.0% before final unload.

Early in the first cycle, the stress-strain dependency is nonlinear and noisy. This transitory stage reflects the accommodation regime between the substrate, the sample and the tip up to ε =3.5%. Then, the curve exhibits an elastic-like behaviour up to ε =9.0% and a true stress of about σ=0.78 GPa. A Young's modulus of about $E_{[001]}$=141.9 GPa is deduced from the early beginning of the first unload. From this point and during the rest of the whole compression test, mobile contrast bands are observed in the nanocube.

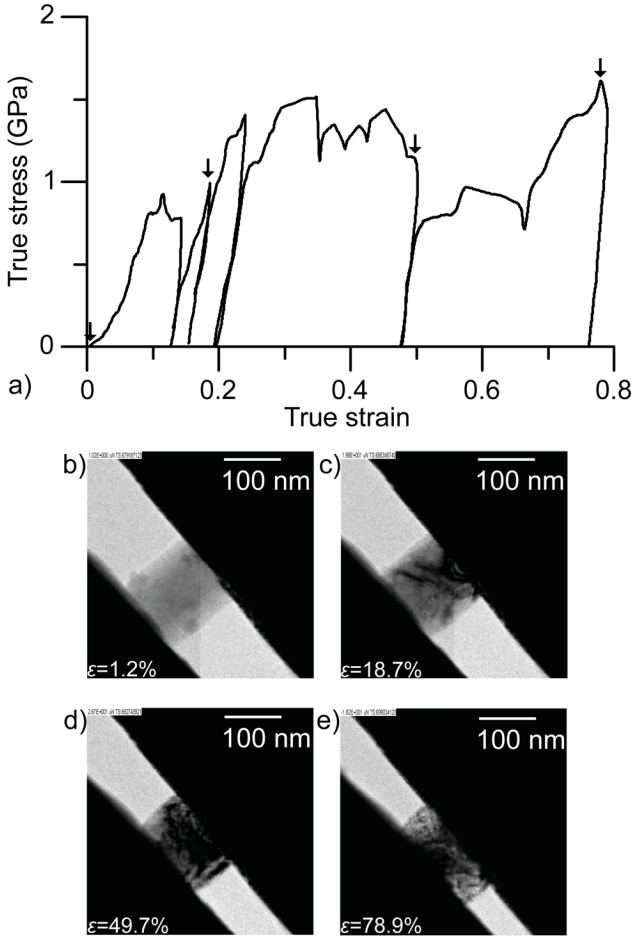

Fig. 2 *(a): Stress-strain curve for a 140 nm edge lengths MgO nanocube compressed in situ. Five loading-unloading cycles are shown. Black arrows refer to snapshots. (b)-(e): Images at ε=1.2%, ε =18.7%, ε =49.7% and ε =78.9% true strain are represented.*

Contrast bands may occur for several reasons *e.g.*, the elastic deformation of the lattice or the presence of mobile/sessile dislocations. In the following, we will focus only on contrast bands that are believed to be the signature of dislocations. These contrast bands may be recognized by their peculiar curved shape as well as their specific orientation *e.g.*, the two angled contrast bands observed on the ε =18.7% image of figure 2. Nevertheless, due to the Bragg conditions, all the defects cannot be observed during the experiment.

One can note that all the residual contrasts accumulated during the first load cycle, up to ε=13.1%, vanish during the first unload. This phenomenon occurs because of both the compressive stress relaxation and the surface image forces, believed to be particularly effective in nanometer-sized samples. This leads to a perfectly refreshed microstructure comparable to the one observed figure 2b.

At ε=18.7%, one may see two freshly nucleated, linear and parallel contrast bands (figure 3c). These bands are tilted of about 45 degrees from the [001] nanocube surfaces what might be an evidence of dislocation glide in {110} slip planes. After their emergence from a surface and/or an edge (the quasi-2D conditions of the experiment precluding a more precised investigation), both traces escape from the opposite side of the nanocube. Further contrast bands can be observed during the third cycle and the beginning of the fourth one where the true stress rises up to σ=1.51 GPa. During the fourth cycle, successive strain bursts take place. Similar strain bursts are often described in the literature [63-66] and are attributed to dislocation nucleation or multiplication peaks and subsequent severe sudden plastic deformation. Although the deformed nanocube becomes very thick during the fourth cycle, these severe plastic deformation events are still recognizable by the high contrast they produce *e.g.*, on the ε=49.7% image (figure 2d). Nevertheless, it is not possible to quantitatively analyse slip contrasts from the middle of the cycle four up to the end of the fifth cycle because of their high density (figure 2e). Finally, the sample is unloaded after the fifth

cycle and a total deformation of about ε=79.0%. No sign of failure has been observed during the unload.

III.2 Focus on the early stages of deformation

In order to investigate further the elementary mechanisms ~~are~~ responsible for the first stages of ~~the~~ MgO nanocubes deformation, we performed two supplementary *in situ* compression tests. Stress-strain curves of 90 and 120 nm edge lengths nanocubes are represented figure 3. As the stress-strain curve main features of *ca.* 100 nm range MgO nanocube have been described in the previous section, we will focus only on new outcomes in the following.

We observe that both samples are characterized by a strain burst occurring at higher stress than in the case of the 140 nm sample. At this point, true stress is about 2.72 and 5.03 GPa, respectively for the 120 and the 90 nm samples. In the inset of figure 3, an image of the 120 nm sized nanocube is shown at ε=7.3% *i.e.*, during the initial strain burst. Once again, we observe an inclined and straight contrast band, tilted of about 45 degrees from the indenter and generated from the surface and/or an edge of the nanocube, similarly to what was observed in the case of the 140 nm sample (figure 2).

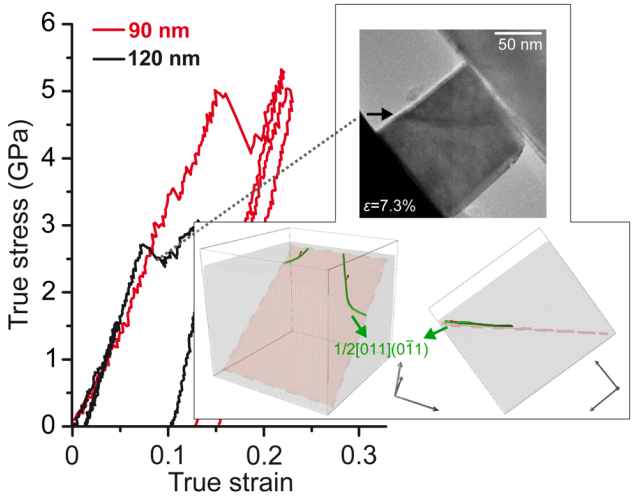

Fig. 3 *(Color online) Stress-strain curves for two MgO nanocubes of 90 (red line) and 120 (black line) nm edge lengths. In the inset: TEM image of a 120 nm sample during*

compression, ε=7.3%. The black arrow shows a contrast band corresponding to dislocations that emerge from the surface of the cube. Two MD simulation snapshots of a 12.6 nm edge lengths nanocube are also represented. Reconstructed ½<110>{110} dislocations are in green. The slip plan is in red. Atoms are shown in transparent light grey for the sake of clarity. The coordinates system is oriented along the cubic directions.

To confirm our hypothesis of {110} glide planes, we performed MD compression tests of MgO Nanocubes. Although the compression rate that can be computed is far higher than in the experiment, and the maximum size of the sample smaller (especially in the case of ionic systems), MD simulations are known to provide a qualitative basis for the identification and interpretation of elementary mechanisms possibly responsible for the deformation of nano-objects [17,67,68]. Figure 3 shows early-nucleated dislocations during the compression of a 12.6 nm edge length nanocube by MD. Here, dislocations are nucleated from ~~the~~ two lateral edges (contrarily to th other top and bottom planar edges) of the nanocube. The slip plane is $(0\bar{1}1)$ and the Nye tensor analysis leads to dislocations characterized by a ½[011] Burgers vector. ½<110> Burgers vectors are characteristic of perfect dislocations in the B1 structure. Similar compression tests have been performed for 10.1, 7.6, 5.9 and 4.2 nm edge length cubes. ~~All the~~ Corresponding stress-strain curves are presented figure 4. They are first characterized by a linear elastic regime up to ε~3%. $E_{[001]}$ values are displayed table 1. In order to compare $E_{[001]}$ to bulk Young's modulus $E_{[001]}^{Bulk}$, bulk elastic constants are calculated. Results lead to C_{11}=282.8 GPa, C_{12}=138.0 GPa and C_{44}=138.0 GPa. These results are in good agreement with recent calculations using the same interatomic potential [50]. We deduced $E_{[001]}^{Bulk}$=192.3 GPa using the anisotropic elastic theory. Afterwards, the elastic regime becomes non-linear up to 10.8%< ε <11.4%, depending the size of the sample. This phenomenon is commonly observed at the nanoscale and is attributed to surface forces and anharmonicity [69,70]**.** The yield stress varies continuously from 40.5 to 35.2 GPa decreasing the size of the sample and dislocations nucleate. Nucleation can be inferred from the

simulated stress-strain curves by the correlated stress drops. When dislocations nucleate (or escape), top or bottom surfaces of the sample are rearranged leading to a slight increase of the distance between the sample top surface and the indenter. As the flat punch force varies inversely with this distance, the stress drops down. The onset of plastic deformation is controlled by ½<110>{110} dislocations only, nucleated either from an edge, a surface or a corner of the nanocube. A detailed analysis of the localization of dislocation nucleation first events is summarized table 1.

Tab. 1 *Young's moduli and yield stresses for MD compression simulations, plus sites and slip systems of the first nucleated dislocations.* E_{Bulk}*=192.3 GPa is deduced from the* C_{ij} *and the anisotropic elastic theory. For the 7.6 nm particle, two dislocations nucleate simultaneously.*

Table 1

Size [nm]	$E_{[001]}$ [GPa] $(E_{[001]}/E_{[001]}^{Bulk})$	Yield stress [GPa]	Dislocation slip system	Nucleation site
4.2	142.7 (0.74)	40.5	$\frac{1}{2}[10\bar{1}](101)$	Top edge
5.9	165.0 (0.86)	37.5	$\frac{1}{2}[10\bar{1}](101)$	Bottom corner
7.6	179.2 (0.93)	36.3	$\frac{1}{2}[101](\bar{1}01)$ $\frac{1}{2}[011](0\bar{1}1)$	Lateral edge Lateral surface
10.1	182.4 (0.95)	35.8	$\frac{1}{2}[101](\bar{1}01)$	Lateral edge
12.5	191.7 (1.00)	34.7	$\frac{1}{2}[011](0\bar{1}1)$	Lateral edge

No dislocation is observed in the {100} or {111} glide planes during the simulations. This result agrees with early 45 degrees tilted contrast bands, described on the TEM images of figures 2 and 3. This confirms that the initial elementary process that governs the deformation of <100>-oriented and pristine MgO nanocubes under uniaxial compression is the nucleation of ½<110> perfect dislocations, gliding later ~~on~~ in {110} slip planes.

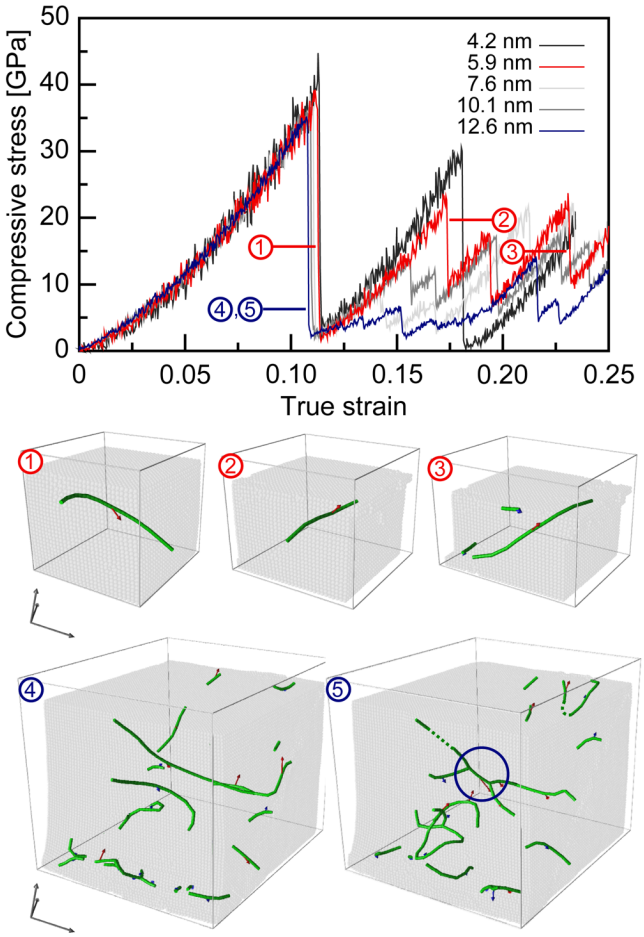

Fig. 4 *(Color online) Stress-strain curves of MgO nanocubes from MD compression simulations. ①-⑤: Images of nanocubes during compression. Green lines correspond to dislocations and red arrows represent ½ <110> Burgers vector orientation. ①-③ show the evolution of the 5.9 nm sample. ④-⑤ show the dislocation organization at the end of the first nucleation peak of the 12.6 nm sample. The blue circle shows a dislocation junction embryo. The coordinates system is oriented along the cubic directions.*

IV Discussion

Only few *in situ* compression experiments have been dedicated to ceramic nanoparticles, especially in the 100 nm range size. Here we present results based on a TEM experimental – MD simulation crossed approach, applied to initially dislocation-free MgO nanocubes.

IV.1 Toward small-size effects on MgO mechanical properties

On the contrary to their bulk counterpart, nanometer-sized MgO particles deform up to large strain, beyond ε=78.9% in the experiment, and no sign of crack has been observed during and after the compression of the nanocubes. These results apply also in the case of MD compression simulation using the Ball and Grimes interatomic potential. In the simulation, we observe a strong effect of the size decrease on the elastic regime. For particles with size lower than 10 nm edge length, $E_{[001]}$ decreases reducing size (table 1). Furthermore, the elastic regime becomes non-linear. This phenomenon is weaker for larger particles and is thus not expected in the experiments (at least for the sizes we investigate here). Nevertheless, $E_{[001]}$ is still lower in the experiment (~142 GPa for the 140 nm particle) compared to the experimental bulk value $E_{[001]}^{Bulk}$~248 GPa [71,72]. We believe that this variation is not a size-effect but may rather be an extrinsic effect as *e.g.*, electron-beam assisted deformation [73-75]. In Zheng *et al.* (2010), the authors point out that the force required to deform amorphous silica (a-SiO_2) nanoparticles at a given elastic strain is lowered by a factor 2 to 3 in the case of electron-beam-on tests compared to electron-beam-off [74]. In Mačković and collaborators (2014), a-SiO_2 nanoparticles are pre-irradiated and then compressed under beam-on/off conditions. Results show that the Young's modulus is increased by a factor 2 (whatever the conditions) compared to the low-dose/beam-off reference conditions with a maximum load force of 50% up to 500% the original one [73]. Similar observations have been made by Zhang and collaborators in crystalline zinc tin oxide NWs where electron-beam irradiation is believed to change elastic and electrical conductivity properties [75]. Nevertheless, despite the fact that similar processes might influence the Young's modulus in our experiments, we believe that they should not modify the elementary mechanisms responsible for plastic deformation.

While we have performed several compression tests, only perfectly aligned and homogeneously deformed samples are presented here. Therefore, alignment should not be a strong source of bias. Furthermore, we did not notice any significant influence of the aspect

size variation, during the deformation of the 140 nm sample, on the subsequent elastic reloads. As a corollary, no effect of the beam exposure time has been deduced from the analysis of elastic reloads. The aspect size effect on the subsequent elastic portions observed in the simulations has also been investigated without significant outcome. More details about this analysis are provided as supplementary information. Finally, the flow stress is also influenced by downscaling, and raises up in comparison to bulk <100>-compression tests at RT *i.e.*, from *ca.* 50 MPa in bulk conditions [24,26,27,76] up to the GPa range for the nanocubes (figures 2 and 3). These results confirm that lowering the scale permits to increase both strength and ductility even for originally brittle ceramics. More specifically, yield stresses from experiments and simulations seem to exhibit a size-effect around 10 and 100 nm. However, the number of experiments should be increased, as the investigated range of size, to get a more significant statistic and further strengthen this hypothesis. In the following, we will further focus on the special features of the plastic deformation regime of MgO nanoparticles.

IV.2 Dislocation nucleation and slip systems in nanosized MgO

Both *in situ* TEM compression tests and MD simulations agree that {110} dislocations are responsible for plastic deformation in the MgO nanocubes. MD compression simulations lead to full ½<110> Burgers vectors. Neither dislocations in the {100} or {111} slip planes nor twinning dislocations were observed in both the experiments and the simulation. ½<110>{110} dislocation glide is also one known mechanism responsible for the deformation of MgO micropillars [77,78] and bulk single crystals [24,26,38,76,79]. Indeed, for <100>-compressions, only ½<110>{110} and ½<110>{111} slip system families may contribute to the deformation. Schmid factor for these slip system families is about $m_{\{110\}}$=0.50 for 4 over 6 ½<110>{110} slip systems and $m_{\{111\}}$=0.41 for 8 over 12 ½<110>{111} slip systems, other being null. Although both slip system families exhibit comparable Schmid factors, ½<110>{111} slip is unfavoured in the case of NaCl-type ionic materials as MgO due to

charge repulsion between ions [80]. This phenomena leads to a surprisingly high shear stress for the {111} slip planes compared to what is generally observed *e.g.*, in FCC metals. With this orientation, {100} slip can only occur in case of misorientations or local rotations. Nevertheless, ½<110>{100} slip is believed to be effective under a rather higher shear stress than ½<110>{110} in RT compression experiments [25,27,79], what does not make {100} slip planes suitable candidates to accommodate deformation in our study.

Although the yield strength in the MD simulations (figure 4) is obviously influenced by the strain rate dependence of dislocation nucleation from the surfaces [67], the role of ½<110>{110} dislocations during the compression of MgO nanocubes is most probably strain rate independent and further constrained by energetic considerations.

To further investigate the relative role of {100}, {110} and {111} glide planes, we have calculated GSF energies using the same interatomic potential than for the MD compression simulations. GSF energies are computed by simply shifting the atoms contained in the upper half of a simulation cell relatively to its lower half by an appropriate translation vector owned by the boundary plan. GSF energies provide a good estimate of the sensitivity of a slip plane to be sheared in a given direction. This concept is frequently used to discuss dislocation-based elementary processes as dislocation core spreading through Peierls-Nabarro approaches [61,81,82] or dislocation nucleation [83-85]. As shown in *e.g.*, Carrez *et al.* (2009) [86], GSF energies calculated in the {110} and the {100} planes of MgO do not exhibit the characteristic, “FCC-like”, stable stacking fault energy (sSFE) what allows ½<110> undissociated dislocations only. This corroborates the results inferred from the Nye tensor analysis during the MD compression simulations where perfect dislocations only are observed (figure 3 and figure 4). Conversely, unstable stacking fault energies (uSFE) can be computed along the Burgers vector direction. The uSFE increases up to a maximum value $uSFE^{max}$ reached for a displacement equivalent to the half of the Burgers vector length (*i.e.*, 1.49 Å). Here we find $uSFE^{max}_{\{110\}}$ =916.7 mJ/m^2, $uSFE^{max}_{\{100\}}$ =2073.1 mJ/m^2 and $uSFE^{max}_{\{111\}}$=2309.4 mJ/m^2. $uSFE^{max}_{\{110\}}$ and $uSFE^{max}_{\{100\}}$ are comparable to *ab initio* calculations

and recent molecular statics simulations using the same interatomic potential [50,86]. While the difference between sSFE and uSFE is often used as an energetic criterion to justify preferred dislocation-based nucleation processes (*i.e.*, partial dislocation, perfect dislocation or twinning) in FCC metallic nano-objects [83], we believe that in the strict case of perfect dislocation, the height of the energetic barrier to produce an elementary shear equal to the Burgers vector (*i.e.*, the $uSFE^{max}$) is a good estimate of the slip plane sensitivity to dislocation nucleation. Here we show that $uSFE^{max}_{\{110\}} < uSFE^{max}_{\{100\}} < uSFE^{max}_{\{111\}}$, what confirms and the occurrence of ½<110>{110} dislocations, and the lack of ½<110>{111} dislocations in the MD compression simulations of MgO nanocubes and thus possibly in the *in situ* TEM experiments. Finally, one can note that $uSFE^{max}$ values are one to two orders of magnitude higher in MgO than the sSFE-uSFE range commonly reached in standard FCC metals *i.e.*, on the range of 10-100 mJ/m^2 [87-89]**,** what might support the extremely high strength observed on the ~~simulation~~ simulated stress-strain curves (figure 4).

IV.3 Deformation regimes and dislocation network

While the nucleation process and the propagation of ½<110>{110} dislocations are at the onset of plastic deformation of initially pristine MgO nanocubes, one interesting thing is to look if dislocation network occur. Figure 5 shows four supplementary TEM images of the 140 nm nanocube (already described in a previous section) during the first load cycle. On this figure, one can identify at least two mechanisms that operate simultaneously. Indeed, red lines on figure 5 emphasize a contrast band that escapes progressively the sample from the surface, just after it nucleates from the other side of the sample. This process of nucleation-exhaustion of dislocations is often observed when dislocation glide is not precluded [10,63]. In some cases, it can be the unique rate-controlling mechanism *e.g.*, in the MD compression simulations for nanocube edge lengths size lower than 10 nm shown figure 4. Indeed, for the 4.2 nm and the 5.9 nm edge lengths simulated samples, stress-strain curves clearly show consecutive stress drops. These peaks are due the nucleation of one or very few dislocations

that induce localized deformation and directly escape from the cube after their nucleation, as observed in figure 4. This dislocation starvation process is less pronounced in the 7.9 nm edge length sample and disappears nearly from the 12.6 nm sample. Actually, in the case of the 12.6 nm sample, deformation is homogeneous and dislocations nucleate from multiple slip systems during the first stress drop. In this case, gliding dislocations intersect and react what can be viewed as the critical step of the dislocation network formation (figure 4). This process is strongly different from the dislocation starvation process described above, as it does not require further dislocation nucleation *i.e.*, dislocations later unlock from the dislocation network and multiply to accommodate further deformation.

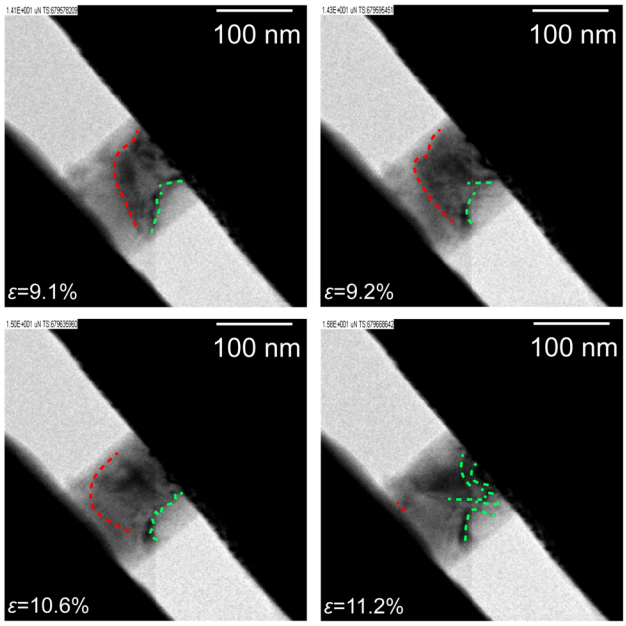

Fig. 5 *(Color online) TEM images of a 140 nm MgO nanocube during the first cycle of load. Dashed red lines show a contrast band that escapes progressively the sample. Green lines show an arrangement of contrast bands that are attributed to the formation of a dislocation network.*

One should note that the lack of subsequent large stress drops on the 12.6 nm sample stress-strain curve is not only due to this last microstructural process but also to the increase of the sample size. Indeed, following a simple first order approach, one can approximate the average shear $\overline{\gamma}$ produced by a {110} gliding dislocation in a cube of edge length l by equation (1):

$$\overline{\gamma} = b\frac{\overline{S}}{V} = b\frac{\sqrt{2}}{2l} \quad (1)$$

Where b is the Burgers vector length, $\overline{S}$ is the averaged {110} surface area swept by the dislocation and V is the volume of the sample. From equation (1), the amount of shear produced by a dislocation decreases as the size of the nanocube increases. As a consequence, and assuming a constant strain rate, the stress response to a shear increment will be smoother for large samples than for small one.

The two deformation regimes described above and their respective transition have already been observed in metallic nano-objects [10,90], and apply thus also to B1-structured ceramics. Further simulations *e.g.*, discrete dislocation dynamics simulations (DDD) [65,91,92], performed at lower strain rates and applied to larger nanocubes should improve our understanding of the effective deformation processes that operate during *in situ* TEM compression tests of MgO nanocubes.

Finally, clear signs of curved dislocations occur during the *in situ* TEM compression tests as in the MD compression simulations. These results are in contradiction with RT TEM observations performed in bulk MgO after compression [33], where dislocation patterns consist merely in long, straight and screw dislocation segments, characteristic of a Peierls lattice friction regime. As the Peierls stress (stress necessary to generate dislocation glide at 0 K) is about 150 MPa in the {110} slip planes and 1600 MPa in the {100} in MgO

[27,76,79,86], we believe that the lattice friction is overcome in both the experiments and in the simulations of MgO nanocube leading to more isotropic dislocation lines.

This topological property is of primary importance because contact reactions between straight screw dislocations may sometimes not lead to the formation of junction locks. This particularly applies in the case of the BCC structure [93] and for the B1 structure of MgO as shown in recent DDD simulations [39]. Actually, non-screw dislocations are required to generate dislocation junction in MgO. Figure 4 shows images of a 12.6 nm nanocube deformed in MD simulations where two curved dislocations with 60 degrees tilted Burgers vectors react to create a junction embryo following the reaction path $1/2\,[10\bar{1}](101) + 1/2\,[01\bar{1}](011) \rightarrow 1/2\,[11\bar{2}](\bar{1}10)$. This local interaction process is not observed in smaller samples where all the deformation is accommodated by only few dislocations that never intersect (figure 4). This result confirms that the probability for dislocation to intersect is more likely in larger samples due to a higher number of defects. Finally, one can see figure 4 that contact interactions between dislocations (*e.g.*, junctions, crossed or repulsive states) enhance the build-up of a dislocation network during the deformation of the 12.6 nm nanocube.

In summary, and in contrary to what is observed in bulk MgO at RT, the high stress reached during the nanocompression tests could allow dislocations to overtake the lattice friction and thus increase the possibility of contact reactions between dislocations. This process improves the formation of a dislocation network, as it is observed in the compression simulations of the 12.6 nm nanocube (figure 4). We believe that a similar process is likewise the source of the persistent contrast bands observed during the *in situ* TEM compression tests (figure 2 and figure 5).

IV.4 Implications for NC ceramics

The results presented above have direct potential future impact for the processing (*i.e.* compaction, ball milling) or the design (*i.e.* mechanical properties) of nanostructured bulk ceramics. Indeed, knowing the plastic deformation mechanisms and mechanical constitutive laws of ceramic nanoparticles are of key importance for phenomena such as third body wear particle in contact mechanics, milling of nanoparticles which may exhibit a plastic behaviour below a certain size, or particle compaction during green body preparation of ceramics. It is for example usually considered that ceramic nanopowders just rearrange without plasticization during compaction [94]. The results presented here for MgO nanocubes and previously for transition alumina nanospheres [14,21] prove that wide plastic flow of ceramic nanoparticles can occur during compaction at RT. This propensity to plastic deformation during compaction opens a new route to deformable ceramics, even at RT. In other words, it would be possible to use plastic deformation of ceramic nanoparticles to obtain green bodies with very high densities and small pores, and sinter them at temperatures well below the ones currently used [95]. Sintering at much lower temperatures would then keep the nanoscale specificities after all the process chain, leading to higher mechanical or peculiar functional properties. This might then apply to orthopaedic devices, with ceramics exhibiting high wear and crack resistance, but also for transparent polycrystalline ceramics for which the quest is today to reach the highest density with the smallest grains [96].

V Conclusion

In summary, we have investigated the mechanical behaviour of <100>-oriented and initially dislocation-free MgO nanocubes using original *in situ* TEM compression tests in the 100 nm size range and MD simulations. Results show high strength as homogeneous and wide deformation without failure. The analysis of TEM contrast bands suggests possible {110} slip. These results are confirmed by the MD compression simulations, in which the nucleation of ½<110>{110} perfect dislocations is at the onset of the plastic deformation. Schmid factor

analysis and considerations based on GSF energy calculations consolidate these results. Dislocations nucleate from edges, corners or surfaces of the nanocubes. In contrary to what is observed in bulk MgO single crystals at RT, dislocations are curved in both the experiment and the simulation, what is due the high stress experienced by the sample during the nanocompression test. This property could enhance the formation of a dislocation network that is generally a high-temperature like process in bulk MgO. Additional simulations and experiments under WBDF diffraction conditions will be conducted to further confirm these results.

Ackowledgements

The authors thank Dr. Philippe Carrez, Dr. Vincent Garnier and Dr. Christoph Begau for useful discussions. The authors acknowledge the Centre Lyonnais de Microscopie (CLYM) for the access to the JEOL 2010F microscope. This work was granted access to the HPC ressources of the FLMSN, "Fédération Lyonnaise de Modélisation et Sciences Numériques", partner of EQUIPEX EQUIP@MESO.

References

[1] Mayo MJ, Hague DC, Chen DJ. Processing Nanocrystalline Ceramics for Applications in Superplasticity. Mat Sci Eng A 1993;166:145–59.

[2] Meyers MA, Mishra A, Benson DJ. Mechanical properties of nanocrystalline materials. Prog Mater Sci 2006;51:427–556.

[3] Narayan RJ, Kumta PN, Sfeir C, Lee DH, Olton D, Choi DW. Nanostructured ceramics in medical devices: Applications and prospects. Jom 2004;56:38–43.

[4] Chevalier J, Gremillard L. Ceramics for medical applications: A picture for the next 20 years. J Eur Ceram Soc 2009;29:1245–55.

[5] Kraft O, Gruber P, Mönig R, Weygand D. Plasticity in confined dimensions. Annu Rev Mater Res 2010;40:293–317.

[6] Minor AM, Morris JW, Stach EA. Quantitative in situ nanoindentation in an electron microscope. Appl Phys Lett 2001;79:1625.

[7] Östlund F, Rzepiejewska-Malyska K, Leifer K, Hale LM, Tang Y, Ballarini R, et al. Brittle-to-Ductile Transition in Uniaxial Compression of Silicon Pillars at Room Temperature. Adv Funct Mater 2009;19:2439–44.

[8] Miller R, Shenoy V. Size-dependent elastic properties of nanosized structural elements. Nanotech 2000;11:139–47.

[9] Gilbert B, Huang F, Zhang HZ, Waychunas GA, Banfield JF. Nanoparticles: Strained and stiff. Science 2004;305:651–4.

[10] Greer J, Nix W. Nanoscale gold pillars strengthened through dislocation starvation. Phys Rev B 2006;73:245410.

[11] Parthasarathy TA, Rao SI, Dimiduk DM, Uchic MD, Trinkle DR. Contribution to size effect of yield strength from the stochastics of dislocation source lengths in finite samples. Scripta Mater 2007;56:313–6.

[12] Korte S, Clegg WJ. Micropillar compression of ceramics at elevated temperatures. Scripta Mater 2009;60:807–10.

[13] Howie P, Korte S, Clegg W. Fracture modes in micropillar compression of brittle crystals. J Mat Res 2012;27:141–51.

[14] Calvie E, Joly-Pottuz L, Esnouf C, Clement P, Garnier V, Chevalier J, et al. Real time TEM observation of alumina ceramic nano-particles during compression. J Eur Ceram Soc 2012;32:2067–71.

[15] Shin C, Jin H-H, Kim W-J, Park J-Y. Mechanical Properties and Deformation of Cubic Silicon Carbide Micropillars in Compression at Room Temperature. J Am Ceram Soc 2012;95:2944–50.

[16] Mook W, Niederberger C, Bechelany M, Philippe L, Michler J. Compression of freestanding gold nanostructures: from stochastic yield to predictable flow. Nanotech 2010;21:055701.

[17] Mordehai D, Lee S-W, Backes B, Srolovitz DJ, Nix WD, Rabkin E. Size effect in compression of single-crystal gold microparticles. Acta Mater 2011;59:5202–15.

[18] Maaß R, Meza L, Gan B, Tin S, Greer JR. Ultrahigh strength of dislocation-free Ni_3Al nanocubes. Small 2012;8:1869–75.

[19] Deneen J, Mook WM, Minor A, Gerberich WW, Carter CB. In situ deformation of silicon nanospheres. J Mat Sci 2006;41:4477–83.

[20] Stauffer DD, Beaber A, Wagner A, Ugurlu O, Nowak J, Mkhoyan KA, et al. Strain-hardening in submicron silicon pillars and spheres. Acta Mater 2012;60:2471–8.

[21] Calvie E, Réthoré J, Joly-Pottuz L, Meille S, Chevalier J, Garnier V, et al. Mechanical behavior law of ceramic nanoparticles from transmission electron microscopy in situ nano-compression tests. Mater Lett 2014;119:107–10.

[22] Carlton CE, Ferreira PJ. In situ TEM nanoindentation of nanoparticles. Micron 2012;43:1134–9.

[23] Takeuchi S, Koizumi H, Suzuki T. Peierls stress and kink pair energy in NaCl type crystals. Mater Sci Eng, A 2009;521:90–3.

[24] Hulse C, Pask J. Mechanical Properties of Magnesia Single Crystals Compression. J

Am Ceram Soc 1960;43:373–8.
[25] Hulse C, Copley S, Pask J. Effect of crystal orientation on plastic deformation of magnesium oxide. J Am Ceram Soc 1963;46:317–23.
[26] Sato F, Sumino K. The yield strength and dynamic behaviour of dislocations in MgO crystals at high temperatures. J Mat Sci 1980;15:1625–34.
[27] Barthel C. Plastiche anisotropie von Bleisulfid und magnesiumoxid (Diploma thesis). University of Gottingen, 1984.
[28] Haasen P, Barthel C, Suzuki T. Choice of slip system and Peierls stresses in the NaCl structure. In: Suzuki H, Ninomiya T, Sumino K, Takeuchi S, editors. Dislocations in solids, Tokyo: University of Tokyo Press; 1985, pp. 455–62.
[29] Tromas C, Girard J, Woirgard J. Study by atomic force microscopy of elementary deformation mechanisms involved in low load indentations in MgO crystals 2000;80:2325–35.
[30] Stretton I, Heidelbach F, Mackwell S, Langenhorst F. Dislocation creep of magnesiowüstite (Mg0. 8Fe0. 2O). Earth Planet Sci Lett 2001;194:229–40.
[31] Li L, Weidner D, Chen J, Vaughan M, Davis M, Durham W. X-ray strain analysis at high pressure: Effect of plastic deformation in MgO. J Appl Phys 2004;95:8357.
[32] Appel F, Bethge H, Messerschmidt U. Dislocation motion and multiplication at the deformation of MgO single crystals in the high voltage electron microscope. Phys Status Solidi A 1977;42:61–71.
[33] Messerschmidt U. Dislocation Dynamics During Plastic Deformation. Berlin, Heidelberg: Springer Series in Materials Science; 2010.
[34] Ikeno S, Furubayashi E. Dislocation Behavior in Pure Niobium at Low Temperatures. Phys Status Solidi A 1975;27:581–90.
[35] Louchet F, Kubin L, Vesely D. In situ deformation of b.c.c. crystals at low temperatures in a high voltage electron microscope Dislocation mechanisms and strain-rate equation. Philos Mag A 1979;39:433–54.
[36] Clauer A, Wilcox B. High temperature tensile creep of magnesium oxide single crystals. J Am Ceram Soc 1976;59:89–96.
[37] Haasen P, Messerschmidt U, Skrotzki W. Low energy dislocation structures in ionic crystals and semiconductors. Mater Sci Eng, A 1986;81:493–507.
[38] Copley S, Pask J. Plastic deformation of MgO single crystals up to 1600 C. J Am Ceram Soc 1965;48:139–46.
[39] Amodeo J, Devincre B, Carrez P, Cordier P. Dislocation reactions, Plastic anisotropy and forest strengthening in MgO at high temperature. Mech Mater 2014;71:62–73.
[40] Duffy T, Hemley R, Mao H. Equation of state and shear strength at multimegabar pressures: Magnesium oxide to 227 GPa. Phys Rev Lett 1995;74:1371–4.
[41] Zerr A, Boehler R. Constraints on the melting temperature of the lower mantle from high-pressure experiments on MgO and magnesioüstite. Nature 1994;371:506–8.
[42] Stankic S, Müller M, Diwald O, Sterrer M, Knözinger E, Bernardi J. Size-Dependent Optical Properties of MgO Nanocubes. Angew Chem Int Ed 2005;44:4917–20.
[43] Takahashi N. Simple and rapid synthesis of MgO with nano-cube shape by means of a domestic microwave oven. Solid State Sci 2007;9:722–4.
[44] Heidenreich R. Electron Reflections in MgO Crystals with the Electron Microscope. Phys Rev 1942;62:291–2.
[45] Cockayne DJH, Ray ILF, Whelan MJ. Investigations of dislocation strain fields using weak beams. Philos Mag A 1969;20:1265–70.
[46] Thölén A. Stress fields at boundaries between contacting particles. J Mat Sci 2006;41:4466–76.
[47] Kagel RO. Infrared Study of the Adsorption of Methanol and Ethanol on Magnesium Oxide. J Chem Phys 1968;49:1638.
[48] Plimpton S. Fast Parallel Algorithms for Short-Range Molecular-Dynamics. J Comput Phys 1995;117:1–19.
[49] Henkelman G, Uberuaga B, Harris D, Harding J, Allan N. MgO addimer diffusion on MgO(100): A comparison of ab initio and empirical models. Phys Rev B

2005;72:115437.
[50] Carrez P, Godet J, Cordier P. Atomistic simulations of 1⁄2<110> screw dislocation core in magnesium oxide (In Press). Comp Mat Sc n.d.
[51] Hardy DJ, Stone JE, Schulten K. Multilevel Summation of Electrostatic Potentials Using Graphics Processing Units. Parallel Comput 2009;35:164–77.
[52] Bitzek E, Koskinen P, Gähler F, Moseler M. Structural relaxation made simple. Phys Rev Lett 2006;97:170201.
[53] Hoover W. Canonical dynamics: Equilibrium phase-space distributions. Phys Rev A 1985;31:1695.
[54] Van Vliet K, Li J, Zhu T, Yip S, Suresh S. Quantifying the early stages of plasticity through nanoscale experiments and simulations. Phys Rev B 2003;67:104105.
[55] Amodeo J, Begau C, Bitzek E. Sup Mat : Atomistic Simulations of Compression Tests on Ni_3Al Nanocubes. Mat Res Lett 2014:1–6.
[56] Begau C. AtomViewer. AtomViewer Free Download at Http://HomepageRuhr-Uni-BochumDe/ChristophBegau/ 2014.
[57] Ackland G, Jones A. Applications of local crystal structure measures in experiment and simulation. Phys Rev B 2006;73:054104.
[58] Hartley CS, Mishin Y. Characterization and visualization of the lattice misfit associated with dislocation cores. Acta Mater 2005;53:1313–21.
[59] Begau C, Hartmaier A, George EP, Pharr GM. Atomistic processes of dislocation generation and plastic deformation during nanoindentation. Acta Mater 2011;59:934–42.
[60] in't Veld PJ, Ismail AE, Grest GS. Application of Ewald summations to long-range dispersion forces. J Chem Phys 2007;127:144711.
[61] Vítek V. Intrinsic stacking faults in body-centred cubic crystals. Philos Mag A 1968;18:773–86.
[62] Gouriet K, Carrez P, Cordier P. Modelling [1 0 0] and [0 1 0] screw dislocations in $MgSiO_3$ perovskite based on the Peierls–Nabarro–Galerkin model. Model Sim Mat Sci Eng 2014;22:025020.
[63] Oh SH, Legros M, Kiener D, Dehm G. In situ observation of dislocation nucleation and escape in a submicrometre aluminium single crystal. Nat Mater 2009;8:95–100.
[64] Kiener D, Minor AM. Source Truncation and Exhaustion: Insights from Quantitative in situ TEM Tensile Testing. Nano Lett 2011;11:3816–20.
[65] Csikor F, Motz C, Weygand D, Zaiser M, Zapperi S. Dislocation Avalanches, Strain Bursts, and the Problem of Plastic Forming at the Micrometer Scale. Science 2007;318:251–4.
[66] Uchic M, Dimiduk D, Florando J, Nix W. Sample dimensions influence strength and crystal plasticity. Science 2004;305:986–9.
[67] Zhu T, Li J, Samanta A, Leach A, Gall K. Temperature and Strain-Rate Dependence of Surface Dislocation Nucleation. Phys Rev Lett 2008;100:025502.
[68] Zhu T, Li J. Progress in Materials Science. Prog Mater Sci 2010;55:710–57.
[69] McDowell MT, Leach AM, Gaill K. On The Elastic Modulus of Metallic Nanowires. Nano Lett 2008;8:3613–8.
[70] Wang YJ, Gao G, Ogata S. Size-dependent transition of deformation mechanism, and nonlinear elasticity in Ni_3Al nanowires. Appl Phys Lett 2013;102:041902.
[71] Durand MA. The temperature variation of the elastic moduli of NaCl, KCl and MgO. Phys Rev 1936;50:449–55.
[72] Chung D-H. Elastic moduli of single crystal and polycrystalline MgO. Philos Mag A 1963;8:833–41.
[73] Mačković M, Niekiel F, Wondraczek L, Spiecker E. Direct observation of electron-beam-induced densification and hardening of silica nanoballs by in situ transmission electron microscopy and finite element method …. Acta Mater 2014.
[74] Zheng K, Wang C, Cheng Y-Q, Yue Y, Han X, Zhang Z, et al. Electron-beam-assisted superplastic shaping of nanoscale amorphous silica. Nat Comm 2010;1:1–8.

[75] Zang J, Bao L, Webb RA, Li X. Electron Beam Irradiation Stiffens Zinc Tin Oxide Nanowires. Nano Lett 2011;11:4885–9.
[76] Amodeo J, Carrez P, Devincre B, Cordier P. Multiscale modelling of MgO plasticity. Acta Mater 2011;59:2291–301.
[77] Korte S, Clegg W. Discussion of the dependence of the effect of size on the yield stress in hard materials studied by microcompression of MgO. Philos Mag A 2011;91:1150–62.
[78] Korte S, Ritter M, Jiao C, Midgley P, Clegg W. Three-dimensional electron backscattered diffraction analysis of deformation in MgO micropillars. Acta Mater 2011;59:7241–54.
[79] Appel F, Wielke B. Low temperature deformation of impure MgO single crystals. Mater Sci Eng 1985;73:97–103.
[80] Gilman J. Plastic anisotropy of LiF and other rocksalt-type crystals. Acta Metall 1959;7:608–13.
[81] Peierls R. The size of a dislocation. Proc Phys Soc 1940;52:34–7.
[82] Nabarro F. Dislocations in a simple cubic lattice. Proc Phys Soc 1947;59:256–72.
[83] Van Swygenhoven H, Derlet PM, Frøseth AG. Stacking fault energies and slip in nanocrystalline metals. Nat Mater 2004;3:399–403.
[84] Rice J. Dislocation nucleation from a crack tip: an analysis based on the Peierls concept. J Mech Phys Solids 1992;40:239–71.
[85] Tadmor E, Hai S. A Peierls criterion for the onset of deformation twinning at a crack tip. J Mech Phys Solids 2003;51:765–93.
[86] Carrez P, Ferré D, Cordier P. Peierls-Nabarro modelling of dislocations in MgO from ambient pressure to 100 GPa. Model Sim Mat Sci Eng 2009;17:035010–1521.
[87] Weinberger CR, Cai W. Plasticity of metal nanowires. J Mater Chem 2012;22:3277.
[88] Mehl M, Papaconstantopoulos D, Kioussis N, Herbranson M. Tight-binding study of stacking fault energies and the Rice criterion of ductility in the fcc metals. Phys Rev, B Condens Matter 2000;61:4894–7.
[89] Zimmerman JA, Gao HJ, Abraham FF. Generalized stacking fault energies for embedded atom FCC metals. Model Sim Mat Sci Eng 2000;8:103–15.
[90] Ryu I, Nix WD, Cai W. Plasticity of bcc micropillars controlled by competition between dislocation multiplication and depletion. Acta Mater 2013;61:3233–41.
[91] Devincre B, Hoc T, Kubin L. Dislocation mean free paths and strain hardening of crystals. Science 2008;320:1745–8.
[92] Bulatov VV, Hsiung LL, Tang M, Arsenlis A, Bartelt MC, Cai W, et al. Dislocation multi-junctions and strain hardening. Nature 2006;440:1174–8.
[93] Kubin L, Madec R, Devincre B. Dislocation intersections and reactions in FCC and BCC crystals. In: Zbib H, Lassila D, Levine L, Hemker K, editors. Multiscale Phenomena in Materials Experiments and Modeling Related to Mechanical Behavior, vol. 779, Warrendale, PA: Materials Research Society Symposium Proceedings; 2003, pp. 25–36.
[94] Oberacker R. Powder Compaction by Dry Pressing. In: Riedel R, Chen I, editors. Ceramics Science and Technology, 2012, pp. 1–37.
[95] Zheng J, Reed JS. Effects of Particle Packing Characteristics on Solid‐State Sintering. J Am Ceram Soc 1989;72:810–7.
[96] Krell A, Klimke J, Hutzler T. Transparent compact ceramics: Inherent physical issues. Opt Mater 2009;31:1144–50.